



Stress behaviors of rib-to-deck double-sided weld detail on orthotropic steel deck

Zhiwen Zhu^{a,*}, Jianpeng Li^b, Xiaowan Chen^a, Alberto Carpinteri^{a,c}

^a Department of Civil and Environmental Engineering, Shantou University, Shantou, Guangdong 515063, China

^b College of Civil Engineering, Hunan University, Changsha, Hunan 410082, China

^c Department of Structural, Geotechnical and Building Engineering, Politecnico di Torino, Italy

ARTICLE INFO

Keywords:

Orthotropic steel deck
Rib-to-deck double-sided weld detail
Stress local effects
Controlled truck loading
Field measurement
FEM

ABSTRACT

To clarify the stress behaviors at a rib-to-deck (RD) double-sided weld detail, controlled truck loading tests were first performed on a newly built long-span cable-stayed bridge with orthotropic steel decks (OSDs). A specifically designed truck loading scheme were employed to simultaneously obtain stress records at the outside weld of the RD detail. A solid FEM panel model was established to determine the stress at the RD double-sided weld detail. It was found that the stress at the detail under wheel loads was dominated by significant local effects, where the apparent stress at the details was produced if their distances to the wheel center were not larger than the rib spacing in the bridge transverse direction or the floorbeam spacing in the bridge longitudinal direction. In addition, each axle could produce an individual stress cycle only when the detail was underneath the deck plate covered by the wheel load distribution width. The FEM results indicated that among the three typically transverse loading locations, the riding-rib-wall loading was the most critical, and generated the highest stress range at the RD double-sided weld detail. The stress range at the outside weld of the detail was higher than that of the inner weld, hence stress measurements outside the detail could conservatively be used for evaluating the fatigue of existing OSD bridges that use the RD double-sided weld detail. The results also provided strong support for the FEM analysis of the OSD using a panel model loaded with a one-sided twin axle.

1. Introduction

It is well known that the ratio of the dead load to all the design loads gradually increases with an increase in the main span of a bridge. To facilitate the construction of bridges with longer spans, it is paramount to reduce the structural dead loads as much as possible, which directly aids in improving the structural efficiency. Orthotropic steel decks (OSDs) are welded structures consisting of deck plates, longitudinal ribs, and floor beams. These are commonly recognized as a lightweight structural system with a high load-carrying capacity, ductility, good shop fabrication control, and expedient construction. Owing to their distinct advantages, OSDs have been widely used in the construction or retrofitting of bridges with various structural forms and different span lengths, particularly long-span cable-stayed bridges and suspension bridges [1].

Engineering practice indicates that it is the fatigue limit state rather than the load-carrying capacity that controls the design of an OSD. There are growing concerns regarding fatigue cracking at the details of an OSD

because of its complicated connections, large number of welds, and weld-induced flaws. Fatigue cracks have appeared at some details of OSDs after years of service [2], more frequently on older bridges with thin deck plates [3]. Fatigue cracks typically appear in the rib-to-deck detail (RD), rib-to-floorbeam (RF) detail, cutout detail, and rib slice [4,5]. Because the deck plate is directly subjected to wheel loads and high stress, with an RD detail experiencing millions of loading cycles during its service life, fatigue cracking can easily occur if the detail is poorly designed, ill-fabricated, or heavily overloaded [2].

For traditionally designed OSDs using close ribs, the RD detail can only be fabricated with a single outside grooved weld. As shown in Fig. 1, four types of cracks may appear on the single-sided RD welds. Crack types 1 and 2 initiate at the weld toe and propagate along the deck plate thickness or rib wall thickness, respectively. Because such cracks appear on the outer surface of the RD detail, they can be easily found during a bridge inspection. However, if full penetration is not employed in the RD detail, this single-sided grooved weld creates a notch at the weld root, which is highly dependent on the amount of weld penetration

* Corresponding author.

E-mail address: zhuzw@stu.edu.cn (Z. Zhu).

<https://doi.org/10.1016/j.jcsr.2021.106947>

Received 25 June 2021; Received in revised form 27 August 2021; Accepted 8 September 2021

Available online 14 September 2021

0143-974X/© 2021 Elsevier Ltd. All rights reserved.

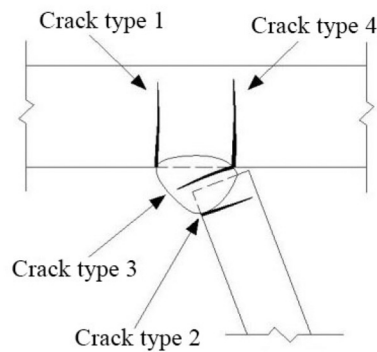


Fig. 1. Crack types of RD single-sided weld detail.



Fig. 2. Profile of RD double-sided weld detail with full penetration.

and the gap size between the rib leg and deck plate. Under wheel loads, the notch presents a severe stress concentration and hence fatigue cracks may initiate at the RD weld root, as the crack types 3 and 4 shown in Fig. 1. The former may propagate through the weld throat, and may only be found after the weld is completely cracked, while the latter may propagate through the deck plate thickness until it reaches the top surface of the deck plate, which is invisible to human-eye inspection at the early propagation stage. Because such through-thickness cracks will lower the deck plate stiffness and damage the structural integrity, overlay debonding and cracking will then appear on the roadway. Consequently, rainwater may leak into the OSD, which may threaten the bridge's serviceability or even present serious social and economic concerns for public transportation systems.

It was found that increasing the amount of weld penetration could decrease the local stress-intensity factor at the weld root [6] and prevent root-to-throat fatigue cracks [7], which could help enhance the fatigue performance of the RD detail. It has been reported that if an 80% weld penetration rate is guaranteed and fatigue cracking still occurs, it will appear at the weld toe rather than at the weld root [8]. It has also been reported that a 100% weld penetration rate produces a slightly lower fatigue resistance than a shallower weld penetration rate such as 80% [9]. However, weld melt-through may occur at a 100% weld penetration rate, which may facilitate the crack initiation under fatigue loads; hence, the RD detail will also have a slightly lower fatigue strength than at the 80% weld penetration rate [10]. Therefore, various specifications require a minimum weld penetration rate of 75% or 80% in the RD detail [11–13]. However, this minimum requirement may not always be guaranteed because of the complicated welding procedure. Hence, RD details with different weld penetration rates may present different crack modes, with some reported cracks appearing at the weld toe [14], other cracks occurring at the weld root [15], and some mix results reported at the RD detail [9,16].

The RD double-sided weld joint, in which a fillet weld was added to the inner side of the RD weld connection, was recently developed for the fabrication of the OSD in bridge engineering. Its weld profile can be partial or full penetration (Fig. 2). Compared to the RD single-sided weld joint, the inner and outside welds at the RD double-sided weld joint provide a stronger connection between the deck plate and the rib wall. The double-sided weld joint tends to improve the fatigue resistance of the RD detail by increasing the weld depth and reducing weld defects, out-of-plane deformation, and particularly the stress concentration [17]. Consequently, the stress concentration and stress-intensity factor (SIF) at the weld root may be reduced.

The double-sided weld technology for the RD detail has been employed in the construction of several long-span bridges in China, including the Zhuankou Yangtze Highway Bridge [18] and the Shishou Yangtze River Bridge [19], although few studies have been carried out on their stress behavior and fatigue performance. Zhang [20] investigated the fatigue crack propagation behavior of the RD double-sided weld detail using the finite element method (FEM) and fracture mechanics and found that the fatigue crack propagation was a mode I-dominated mixed mode. They further studied the fatigue failure mode of this RD detail with cracks initiated at the weld root, and found that an increase in the weld penetration rate could significantly decrease the equivalent structural stress range. Meanwhile, if the weld penetration rate exceeded 75%, the stress range at the weld root was still lower, and the fatigue performance at the RD double-sided weld detail was controlled by the fatigue failure mode, with cracks initiated at the weld toe. Luo [21] evaluated the notch stress at this detail through FEM modeling and found that the maximum notch stress range at an RD double-sided weld detail decreased by 19.1% compared to that at an RD single-sided weld detail. It was also found that the effects of the weld penetration rate on the fatigue performance were not as significant as those for the RD single-sided weld detail. Based on an FEM analysis, Liu [22] investigated the SIF at the crack tip of RD single-sided and double-sided weld details, and found that the SIF at the tip of the RD double-sided weld detail was significantly lower than that of the single-sided weld detail. Hence, the fatigue performance of the RD double-sided weld detail was improved.

Compared to the extensively studied traditional RD single-sided weld detail for an OSD, as introduced above, there are limited reports on the RD double-sided weld detail. Due to rapid application of this detail to several bridge projects, several tests have been carried out to compare its fatigue resistance with the RD single-sided weld detail. You [23] incorporated the RD single- and double-sided weld details in the same fatigue models, which consisted of only one or two ribs in transverse direction and was only 400 mm in longitudinal direction. The test under cyclic loading found that the RD double-sided weld detail provided a significant higher fatigue life than that of the RD single-sided weld detail. Based on the Shenzhen-Zhongshan Link Project, Zhang [24] tested full scale OSD models fabricated with RD single- or double-sided weld detail. The study indicated that the RD double-sided weld detail also presented high fatigue resistance than that of the RD single-sided weld detail, and the fatigue cracking mode switched from cracking at weld root of the RD single-sided weld detail, to cracking at inner weld toe of the RD double-sided weld detail. Zhang [25] used the FEM-based equivalent structural stress method to further investigate the fatigue performance of the RD double-sided weld detail. They concluded that the fatigue failure is dominated by weld toe cracking when the welding penetration rate is higher than 75%, and an increase in weld size would improve the fatigue resistance of weld toe cracking.

The RD double-sided weld detail is considered as an innovative technology in China, and more and more newly designed bridges employ this detail. Compared to its widespread engineering practice, above-mentioned few studies were only limited on fatigue performance through model tests or FEM analysis, and hence they were not enough to cover maintain and evaluation of existing bridge using the innovative RD weld detail. Meanwhile, the stress behavior at the RD double-sided

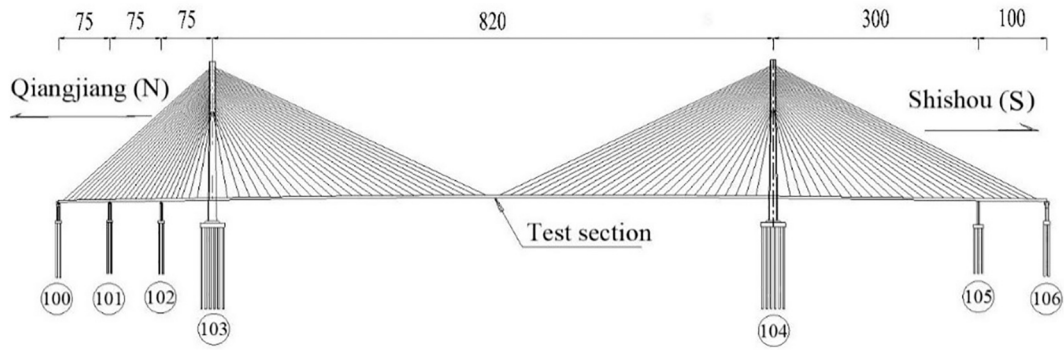


Fig. 3. Elevation layout of Shishou Yangtze River Bridge (Unit: m).

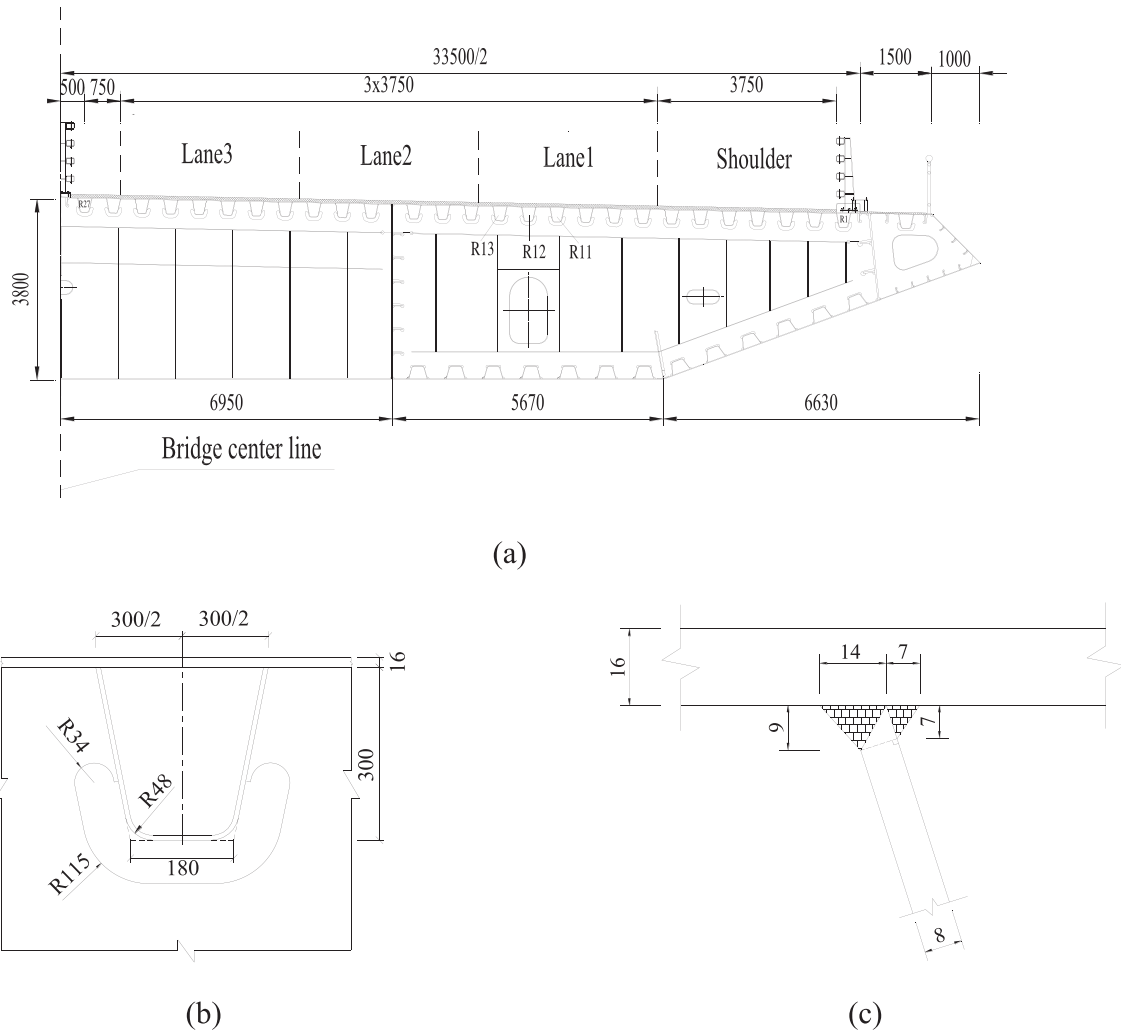


Fig. 4. Typical structural layout (Unit: mm): (a) steel box girder; (b) RD double-sided weld; (c) RD double-sided weld.

weld detail, particularly at the inner side fillet weld in comparison with outer side weld detail, is not clear under the passage of trucks, which will be a major concern for bridge engineering but can be effectively addressed based on actual bridge measurement and FEM analysis.

Because of their ability to truly represent the structure, connection details, and welding procedures for a real bridge, as well as the weight and configuration of trucks, field tests such as controlled truck loading [8] and field monitoring under random traffic flow [26] are commonly recognized as the most realistic and effective way to investigate the

stress behavior at the fatigue critical details of an OSD. In this study, the stress at an RD double-sided weld detail of an OSD was investigated through on-site controlled truck loading tests and FEM analyses. Then, the stress behaviors of details at different transverse locations were compared with each other under various transverse wheel loads. It should be noted that the fatigue evaluation of the RD double-sided weld detail will not be the focus of this study.

Table 1
Weight information of loading truck.

Front axle (t)		Middle axle (t)		Rear axle (t)	
7.21		11.24		11.70	
Left wheel	Right wheel	Left wheel	Right wheel	Left wheel	Right wheel
3.43	3.78	5.45	5.79	6.03	5.67

gauges applied at an RD detail of the real bridge. The gauges were then connected to a DH3820 data acquisition system, which was mounted inside the box girder and was close to the test section.

3.2. Truck loading scheme

The present test was conducted on August 30, 2019, on the Shishou Yangtze River Bridge. The weather forecast indicated a partly cloudy day, with minimum and maximum temperatures of 21 °C and 33 °C, respectively, and a gentle northeast wind at the bridge site.

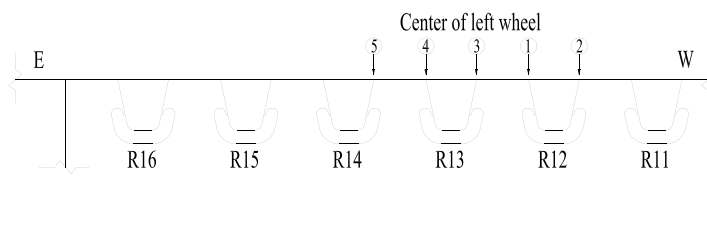
1) Loading truck information

The loading truck for the on-site test was a Dongfeng-153 truck with three axles. The axle spacing and wheel spacing are shown in Fig. 7. The distance between the front and rear axles was 3.8 m, which was larger than the floorbeam spacing (3 m). Because the spacing between the middle and rear axles was only 1.4 m, which was significantly shorter than the floorbeam spacing, they could be recognized as a twin axle group. The truck weighed 30.15 t. Table 1 lists the weight of each axle and its individual wheels. Only a slight weight difference was observed between the left and right wheels.

2) Loading schemes

The controlled truck loading tests consisted of truck crawl and truck dynamic tests. In the crawl test, the truck moved slowly at a speed of approximately 2 km/h, with the left wheel of the rear axle centered at and passing the specified location. In order to obtain stress response at RD details at different transverse location, which can reflect the effects of their distance to the wheel center, loading cases LC1-LC5 are arranged and illustrated in Fig. 8 (a). They were considered the most critical transverse loading cases for the RD detail [2], and loading case LC1 was used for both the crawl test and dynamic test. It can be seen that cases LC3-LC5 gradually became farther away from R12. Fig. 8 (b) shows the truck wheel position on the bridge deck for LC1.

The crawl tests were carried out under the passage of truck with a very low velocity of about 2 km/h. Since the truck moved so slowly, dynamic loading effects were assumed to be negligible [28]. In the crawl tests, loading truck headed south in the longitudinal direction of the bridge, with its rear axle directly centered at floorbeam N3 and the left wheel centered at the specified location shown in Fig. 8 (a). Then, the truck engine was turned off, followed by the initiation of the data acquisition system. Next, the truck engine was turned on, and was



(a)



(b)

Fig. 8. Truck loading: (a) loading cases; (b) wheel positioning.

allowed to move slowly to the south, while the data acquisition system obtained measurements. Subsequently, the truck passed the instrumented RD detail, went straight to a position that was not less than 50 m away from the test section, and finally stopped. Because the truck speed was very slow, the sampling frequency was set to 10 Hz.

The dynamic test was designed to capture the impact effects of truck loading on the stress at RD detail, with a truck speed of approximately 40 km/h [28]. In this test, the test truck also headed south with its front axle 100 m away from the test section, as shown in Fig. 5. First, the data acquisition system was initiated and then began sampling. The truck moved to the south and passed the instrumented RD detail, directly reached a position that was over 100 m from the test section, and finally stopped. With this moderate truck speed, the sampling frequency was changed to 100 Hz, and the dynamic effect of the truck loading had to be considered.

3.3. Results of truck loading tests

Considering the tire contact area shown in Fig. 7, the load distribution function of an asphalt wearing surface with a thickness of 70 mm, and a load dispersal angle of 45° to the vertical, the wheel load distribution width on the deck plate in the transverse direction of the bridge increased to 640 mm, which was slightly larger than the rib center-to-center spacing (600 mm), as shown in Fig. 9. Hence, the wheel loads on the top surface of the deck plate would cover an area of 340 mm × 640 mm for both the middle and rear axles, and it was clear that this coverage scale was wider than the rib center-to-center spacing in the bridge transverse direction.

Because no strain gauges were installed at the inner side of the RD detail, the results discussed in this section are based on the stress simultaneously measured at the outside weld of the test RD double-sided weld detail.

1) Loading case LC1

(1) Crawl test

The crawl test was specifically designed to measure the stress at the RD detail after gradually unloading the truck from the test section, and

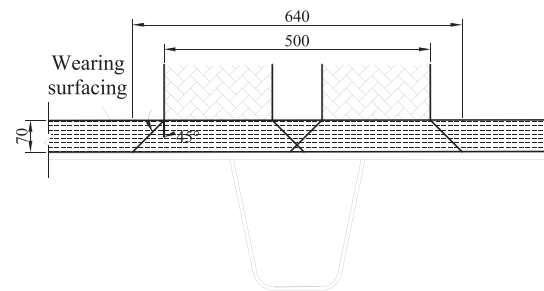


Fig. 9. Wheel load distribution width in bridge transverse direction (Unit: mm).

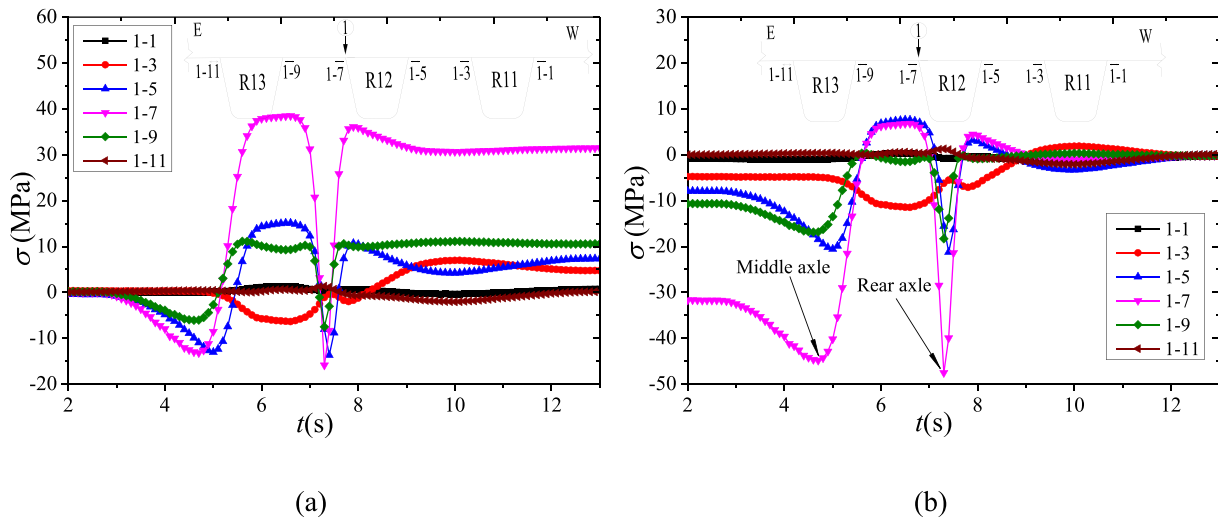


Fig. 10. Stress records at RD-D under LC1: (a) gauge records; (b) actual stress.

to obtain the stress ranges at different locations after data processing. Such a loading regime could help position the truck wheel more accurately at the specific loading location.

Fig. 10 (a) presents the stress time histories at the deck plate side of the RD detail (RD-D) after the truck started at floorbeam N3, passed the RD detail, and finally traveled to the south. Based on the axle spacing between the middle and rear axles, as well as the time interval indicated at gauge 1-7, the estimated truck traveling speed was 1.9 km/h. It was certainly very slow, as desired.

It should be noted that for this specifically designed crawl test, the first recorded stress time histories, as shown in Fig. 10 (a), were not the actual stress responses at the RD detail. When the data acquisition system was initiated, all the channels were cleared to zero, but the truck had already placed a load on the details. Hence, the recorded stress time histories were the stress responses at the RD detail during the truck unloading. Hereafter, these are called the gauge records. It can be understood that after the truck traveled away from the detail, the stress at the measured details gradually became smaller, and eventually became negligible when the truck was far away from the test section. As shown in Fig. 10 (a), when $t > 12$ s, the gauge records are steady and smooth, which means that the truck was already far away from the gauges, and the test section was completely unloaded. With this consideration, the gauge records at $t = 12$ s were treated as constants, and the actual stress time histories at the RD details were obtained by subtracting these constants from their gauge records. Hence, the gauge records after $t = 12$ s would be zero because of the absence of loading effects. Fig. 10 (b) plots the actual stress records at RD-D after data processing.

To understand the stress time histories in Fig. 10 (b), the curves can be read from right to left, imagining the truck backing from the south to the north, with the rear and middle axles subsequently passing the test section, and eventually stopping at a position centered on floorbeam N3, as shown in Fig. 5. Because the middle axle's weight was very close to that of the rear axle, these axles produced almost equal stress peaks in Fig. 10 (b), which validated the effectiveness of the crawl test.

Gauge 1-7 on the deck plate side, which was directly underneath the wheel center, produced the maximum stress response, with a peak tensile stress of 6.8 MPa and maximum compressive stress of 48.8 MPa. The stress responses at gauges 1-5 and 1-9 were less than that at 1-7, with a further decrease at 1-3. The stress records from gauges 1-1 and 1-11 were very small and negligible. The stress ranges at gauges 1-7, 1-5, 1-9, 1-3, 1-11 and 1-1, calculated using the maximum stress subtracted by the minimum stress on the stress curves, were 55.6 MPa, 28.8 MPa, 18.7 MPa, 13.4 MPa, 3.4 MPa, and 1.7 MPa, respectively, as shown in Fig. 11. The abscissa in Fig. 11 is defined as the gauge distance

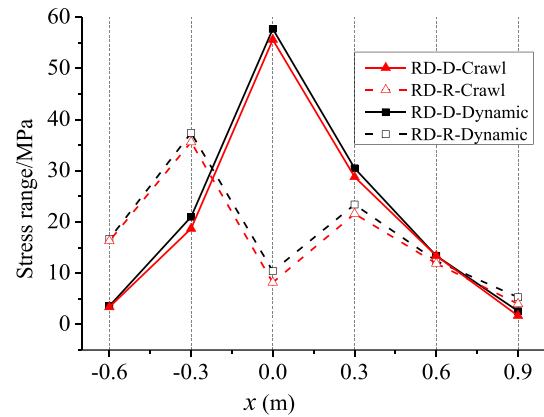


Fig. 11. Stress ranges at RD detail under LC1.

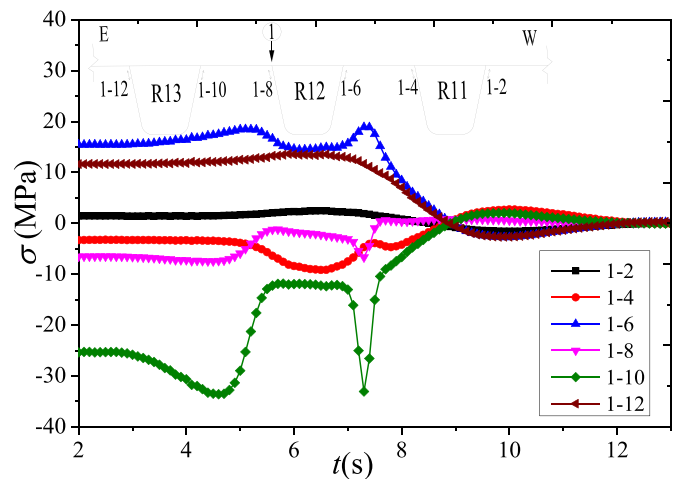


Fig. 12. Stress records at RD-R under LC1.

to the wheel center and is positive if the gauge is on the west side of the wheel center. It is clear that the stress range at the RD detail decreases with the increase of its distance to the wheel center, and when the distance of RD detail to the wheel center is beyond one rib spacing (0.6 m), the stress range at this detail will be low.

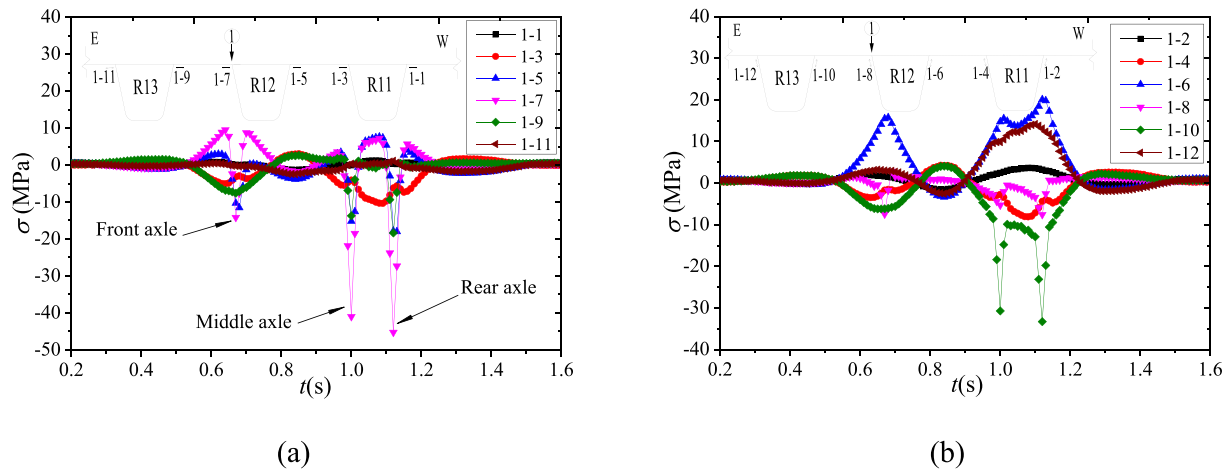


Fig. 13. Stress records at RD detail in dynamic test: (a) deck plate side; (b) rib wall side.

Because of the space limitations of this paper, hereafter, the gauge records at the RD detail will no longer be presented. Fig. 12 shows the actual stress time histories at the rib wall side of the RD (RD-R). The stress at gauge 1–10 is the highest, with a stress range of 35.6 MPa. The stresses at gauges 1–6 and 1–12 are slightly low, with stress ranges of 21.6 MPa and 16.3 MPa, respectively. Although gauge 1–8 was directly underneath the wheel center, its stress response was as low as that of gauge 1–4, while truck loading produced negligible stress on gauge 1–2.

As observed in this loading case, when the RD detail was close to the wheel center, the stress at the detail will be large. However, if it was far from the wheel center, its stress was small. In more detail, if the distance to the wheel center exceeded the spacing between ribs (0.6 m), the stress ranges at those details were low. Hence, the RD detail showed significant local stress effects under wheel loading.

(2) Dynamic test

In the dynamic test, the left wheel was required to exactly pass the same transverse location as in the crawl test. It was carried out to obtain full stress curves and investigate the dynamic effects at the RD detail under the passage of a truck with moderate speed.

The stress time histories at the RD detail in the dynamic test are plotted in Fig. 13. For the RD-D directly underneath the wheel center, gauge 1–7 produced the maximum stress out of all the gauges on the deck plate side. It agreed well with the results from the crawl tests. In addition, three individual compression peaks were clearly identified at gauges 1–5, 1–7, and 1–9. Referring to Fig. 9, it is clear that these gauges were covered by the wheel load distribution width on the deck plate in the bridge transverse direction. The three peaks at gauge 1–7 corresponded to the front, middle, and rear axles of the truck, as shown in Fig. 13 (a). Based on the distance between the front and middle axles, and their time passing the detail, the calculated truck speed was 41.8 km/h, which was very close to the desired truck travel speed of 40 km/h.

The stress curves from the dynamic tests, and particularly the peaks produced by the middle and rear axles (from 1.05 s to 1.5 s), look very similar to the stress records from the crawl test. The peak tensile and compressive stresses at gauge 1–7 were 9.5 MPa and 48.2 MPa, respectively, resulting in a stress range at gauge 1–7 of 57.7 MPa, which was slightly higher than the stress range of 55.6 MPa in the crawl test. The stress ranges at gauges 1–1, 1–3, 1–5, 1–9, and 1–11 were 2.6 MPa, 13.4 MPa, 30.5 MPa, 21.0 MPa, and 3.6 MPa, respectively, which were also very close to the results from the crawl tests, as plotted in Fig. 10.

For the stress at the rib wall side, Fig. 13 (b) shows that the maximum stress range did not appear at gauge 1–8, which was directly underneath the wheel center. Instead, gauge 1–10, which was on the closest RD detail on the neighboring rib, generated the highest stress range of 37.4

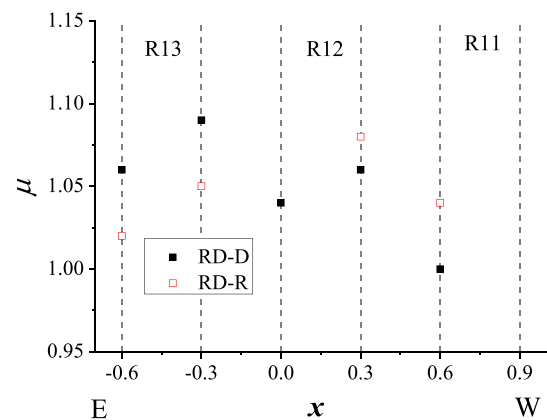


Fig. 14. Dynamic load allowance at RD detail.

MPa, which also agreed well with the results from the crawl test. The stress range at gauge 1–8 was only 10.4 MPa, which was significantly lower than that of gauge 1–10. In addition, the stress ranges at gauges 1–2, 1–4, 1–6, and 1–12 were 5.3 MPa, 12.4 MPa, 23.4 MPa, and 16.7 MPa, respectively. Fig. 11 compares the stress ranges of all the gauges between the dynamic and crawl tests. The agreement indicates that the present crawl test method was successful in obtaining the stress response of the RD detail.

Fig. 13 also confirms that when the distance from the RD detail to the wheel center did not exceed the rib spacing, high stress was produced at that detail, whereas if the distance exceeded the rib spacing, the stress response at the detail was low.

Based on the measured stress ranges from both the crawl test and dynamic test, the dynamic load allowance, which reflects the dynamic loading effects on the OSD, can be defined as follows:

$$\mu = 1 + \frac{\sigma_r' - \sigma_r}{\sigma_r} \tag{1}$$

where μ is the dynamic load allowance; and σ_r' and σ_r are the stress ranges in the crawl and dynamic tests, respectively.

Fig. 14 plots the dynamic load allowance at both the deck plate side and rib wall side of the RD detail. Because of the very small stress range at the rib wall side directly underneath the wheel center ($x = 0$ m), as well as the small stress range when $x = 0.9$ m, their dynamic load allowance is not provided. The maximum and minimum dynamic load allowance were 1.09 and 1.0, respectively, with an average value of 1.05, which was lower than the value of 1.15 provided in AASHTO LRFD

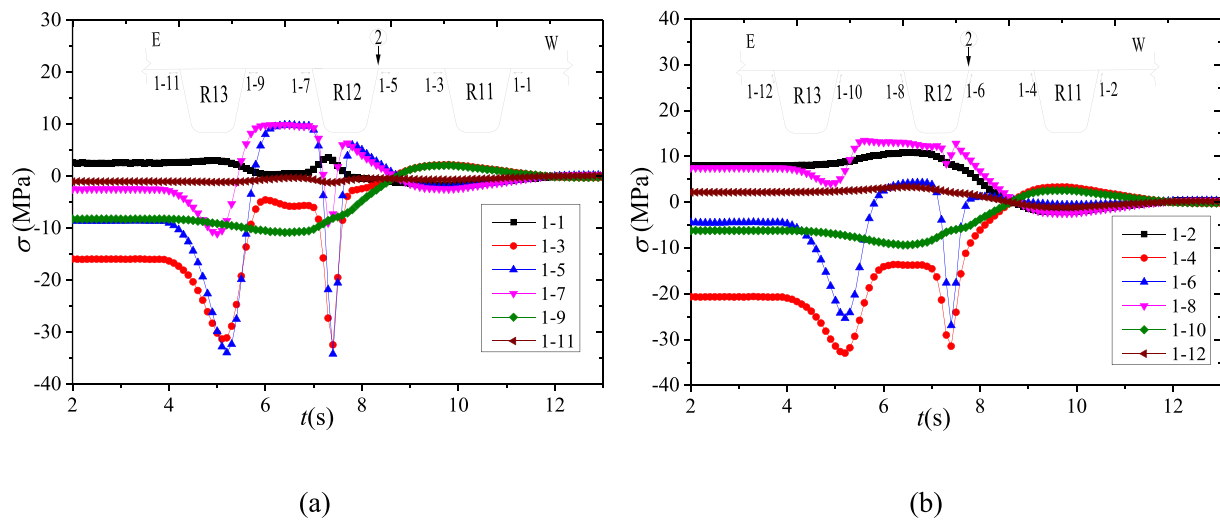


Fig. 15. Stress records at RD detail under LC2: (a) deck plate side; (b) rib wall side.

[11]. It suggests that the dynamic load allowance specified in AASHTO LRFD may be conservative based on stress measurement at the RD detail. However, the dynamic load allowance could be affected by many factors such as the bridge vibration frequency, road surface condition, and truck speed. It was reported that dynamic modulus of the asphalt overlay increases with the loading rate [29], hence its stiffness contribution to the deck system will increase with the increase of the truck speed. Hereafter, the measured dynamic load allowance of 1.05 was used in the FEM analysis.

Because individual stress peaks could be clearly identified at gauge 1–7, the stress influence line in the bridge longitudinal direction could be estimated. Based on the estimated truck speed of 41.8 km/h, the calculated length of the stress influence line ahead of the stress peak, produced by the front axle, as shown in Fig. 13 (a), was approximately 1.5 m. This meant that the apparent stress response could only be produced at gauge 1–7 when the front axle crossed the floorbeam and loaded the instrumented rib span. For the stress records generated by the rear axle, the time corresponding to its peak stress in Fig. 13 (a) was $t_1 = 1.12$ s, and its negligible loading effects started at $t_2 = 1.24$ s. Consequently, the estimated length of the stress influence line after the stress peak produced by the rear axle also equaled 1.5 m, which implied that the apparent stress could only be produced when the rear axle loaded the instrumented rib span. When the rear axle crossed the floor beam and

moved away from the instrumented rib span, the stress could be negligible. Hence, the length of the stress influence line at the RD detail was equal to the floorbeam spacing in the longitudinal direction of the bridge.

2) Loading case LC2

Fig. 15 shows the actual stress time histories measured at the RD details in the crawl tests. The stress curve for gauge 1–5, which was directly underneath the wheel center, shows the highest response under wheel loads. The stress range at gauge 1–5 is 44.1 MPa, while the stresses at gauges 1–3 and 1–7 are slightly lower than that at gauge 1–5, but these three stress curves are all characterized by clearly separated individual peaks. The stress ranges at gauges 1–3, 1–7, and 1–9 are 33.5 MPa, 20.9 MPa, and 12.9 MPa, respectively, while the stress ranges at gauges 1–1 and 1–11 are very small.

As shown in Fig. 15 (b), high stress responses appear at gauges 1–4, 1–6, and 1–8, with stress ranges of 36.3 MPa, 31.2 MPa, and 15.9 MPa, respectively, while very low stress appears at gauge 1–12 because of its large distance from the wheel center. A comparison of the stress ranges obtained at different locations confirmed that if the distance from the RD detail to the wheel center exceeded the rib spacing, the stress response at that detail was low.

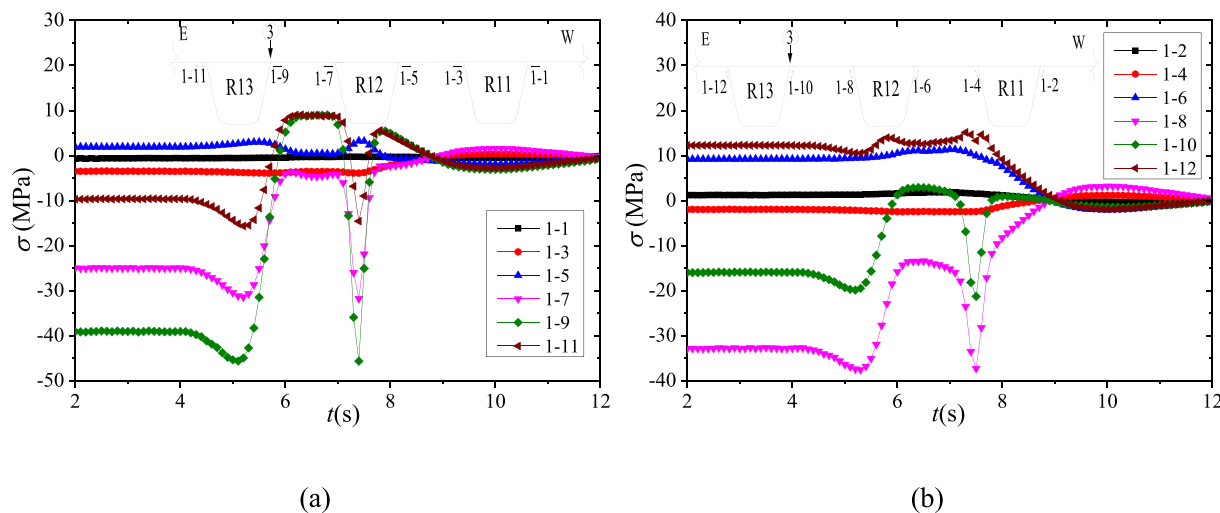


Fig. 16. Stress records at RD detail under LC3: (a) deck plate side; (b) rib wall side.

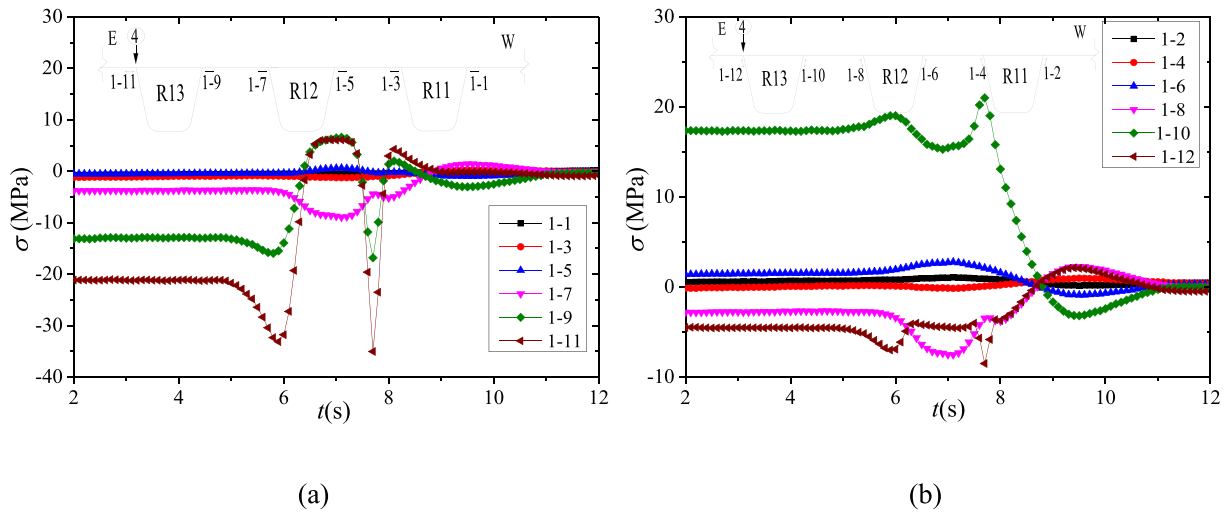


Fig. 17. Stress records at RD detail under LC4: (a) deck plate side; (b) rib wall side.

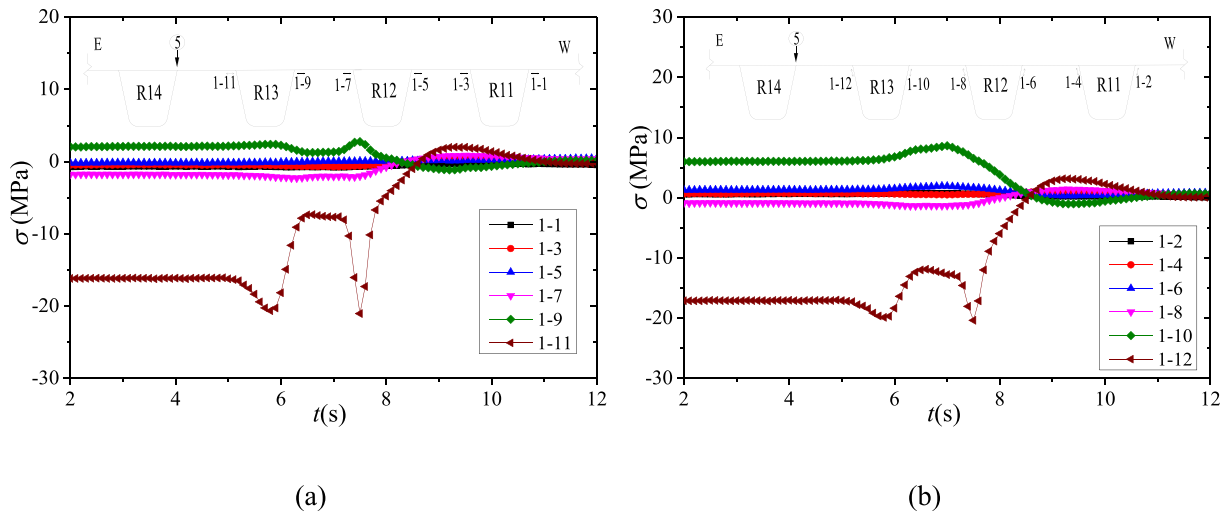


Fig. 18. Stress records at RD detail under LC5: (a) deck plate side; (b) rib wall side.

3) Loading case LC3

The wheel loads then moved to the east side and centered on the RD detail on the west side of R13. The stress responses at the RD details in the crawl tests are shown in Fig. 16. High stresses were produced at the RD details close to the wheel center, such as at gauges 1–7, 1–9, and 1–11 on the deck plate side, and particularly at gauge 1–9, which had the highest stress range of 54.6 MPa because it was directly underneath the wheel center. Meanwhile, high stresses were also produced at gauges 1–8, 1–10, and 1–12 at the rib wall side, with the highest stress range of 40.7 MPa at gauge 1–8. Because the distance from the details on R11 to the wheel center was larger than the rib spacing, the loading effects on gauges 1–1, 1–2, 1–3, and 1–4 were apparently small and negligible.

4) Loading case LC4

Fig. 17 shows the stress curves of the RD details under the passage of the truck at LC4 in the crawl tests. High stresses were present at gauges 1–9 and 1–11 on the deck side, as well as at gauges 1–10 and 1–12 on the rib wall side, because these gauges were located close to the wheel center. The maximum stress range on the deck side was 41.1 MPa at gauge 1–11, while at the rib wall side, the maximum decreased to 24.2 MPa at gauge 1–10. It is clear that the stress ranges at the west-side

gauges decreased with an increase of their distance from the wheel center. Thus, the stress at the R11 detail was very small and hence was negligible.

5) Loading case LC5

When the wheel loads moved further toward the east side of R12 in the crawl tests and centered on the RD detail on the west side of R14, most of the gauges presented low stress responses during the truck passage, as shown in Fig. 18. Both gauge 1–11 on the deck plate side and gauge 1–12 on the rib wall side, which were the closest gauges to the wheel center, showed relatively large stress responses, with stress ranges of 23.0 MPa and 23.5 MPa, respectively. This clearly showed that the stresses at those gauges gradually decreased with an increase in the distance between the gauges and the wheel center. More specifically, when the gauge distance to the wheel center was larger than the rib spacing, the gauges exhibited low stress responses. In particular, the stresses on the gauges applied around R11 and R12 were negligible. This clearly demonstrated the significant local stress effects of the RD detail under wheel loading.

The measurements made it apparent that the stress response at the RD detail was large when it was close to the wheel center, and it decreased with an increase in the distance from the wheel center. More

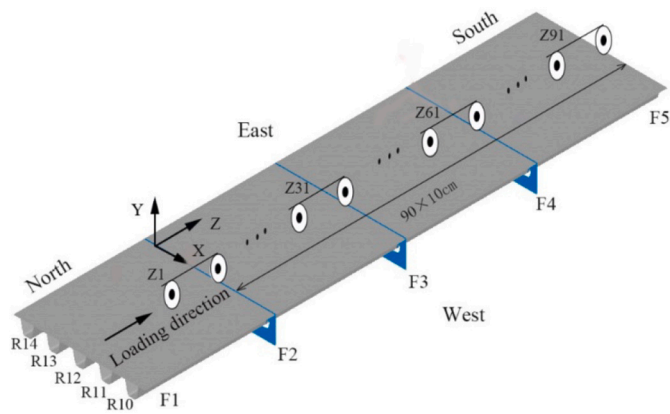


Fig. 19. FEM model of OSD panel.

specifically, if the detail was directly underneath the wheel center, notable stress was produced, and clear individual stress peaks could be observed, such as 1–7, 1–5, 1–9 and 1–11 in LC1, LC2, LC3 and LC4, respectively. If the distance from the RD detail to the wheel center was smaller than the spacing between the ribs, a large stress was produced at the location, such as 1–5 and 1–9 in LC1, 1–3 and 1–7 in LC2, 1–7 and 1–11 in LC3, 1–9 in LC4, as well as 1–11 in LC5. However, if the distance was beyond one rib spacing, the stress response at this location was significantly small, such as 1–1 in LC1, 1–11 in LC2, 1–1 and 1–3 in LC3, 1–1, 1–3 and 1–5 in LC4, as well as 1–1, 1–3, 1–5 and 1–7 in LC5. This observation could also be found at rib wall side, despite the fact that when the RD-R was directly under the wheel center, the rib wall partly acted as a compressive bar due to its directly support to part of the wheel load. Consequently, the stress range at this RD-R was lower compared to that of other RD-D where the rib wall was under bending. Hence, the RD detail showed significant local stress effects under the wheel loading.

Based on the above conclusions, it can clearly be seen that for a passing truck, the stress at the RD detail generated by one side of the wheel will not be superimposed on that from the other side of the wheel. In particular, the loading effects on the RD detail produced by trucks running side-by-side can be ignored.

4. Stress behavior investigated using FEM analysis

For the RD double-sided weld detail, because of the lack of access to the inner side of the rib, no stress gauges could be applied to the inner side of the weld of the RD detail in the field tests. Hence, the stress behaviors at the inner side of the weld were unclear. However, determining the stresses at both the inner side and outer side of the weld was important to comprehensively determine the stress features. It was also important to further investigate the fatigue performance of the OSD using the RD double-sided weld detail. With this consideration, an FEM panel model that used solid elements to accurately represent the RD double-sided weld based on the bridge design drawing was established in ANSYS to obtain the stresses at various transverse locations, similar to

the field test.

The calculated stress results at the RD outer side of the weld were first compared to the field measurements to validate the effectiveness of the FEM analysis. Then, the stress at the inner side was determined and compared to that at the outer side of the RD detail, which further clarified the local stress effects at this detail. Finally, the structural deformation of the OSD, particularly at the RD double-sided weld detail, was determined to assist in understanding the stress behaviors at different truck loading locations.

4.1. FEM model

As shown in Fig. 19, an FEM panel model that consisted of five longitudinal ribs, three floorbeams, and a four-span deck plate was established in the ANSYS software using solid elements. The structural layout was based on the design drawing of the OSD of the bridge, which was accurately represented by the panel model, including the fatigue-prone details such as the RD double-sided welds, RF welds, and floorbeam-to-deck plate welds. The RD double-sided welds in FEM were created by the full penetration weld, with weld size shown in Fig. 4 (c).

In the panel model, the ribs were numbered from west to east, while the floorbeams were numbered F1 to F5 from north (N) to south (S). A coordinate system at the deck plate level, with its origin located at the intersection of F2 with the center line of R14, is shown in Fig. 19. The model was 12 m long in the bridge longitudinal direction (Z), 3 m wide in the bridge transverse direction (X), and 0.616 m high in the vertical direction (Y). The limited model width in the transverse direction was based on the conclusion from the controlled truck tests that the RD detail showed significant local stress effects from wheel loads. Meanwhile, because a solid-web diaphragm was used in this box girder, only the portion of floorbeam above the horizontal stiffeners was modeled, which could help avoid a very large model scale while guaranteeing acceptable accuracy [30].

The Solid45 element in ANSYS, which is a three-dimensional brick element with eight nodes, each having three translational degrees of freedom, was employed to discretize the OSD panel model. Due to its low contribution to the OSD's stiffness at the test temperature condition, the 70 mm thick asphalt overlay on top of the OSD was not modeled, while its load distribution function was considered. In this study, the steel was considered as linear-elastic one, with Young's modulus and Poisson's ratio of 2.06×10^5 MPa and 0.3, respectively.

In order to ensure good control of the mesh quality such as the element edge ratio and aspect ratio, structured meshes were created in most areas of the model, as shown in Fig. 20. Because fatigue-prone details always present stress concentrations at the weld toes, very fine meshes were provided in the areas close to the weld toes. At the RD detail, the first element height normal to the weld toe measured 1.6 mm. Close to the free edge of the cutout, the first element measured 2 mm in its normal direction, whereas at the RF detail, the minimum edge size was 3 mm close to the weld toes (Fig. 20 (b)). Two layers of uniform elements were created in the plate thickness direction, such as for the deck plate, rib wall, and floorbeam web. Consequently, there were approximately 1.54×10^6 elements in the FEM model.

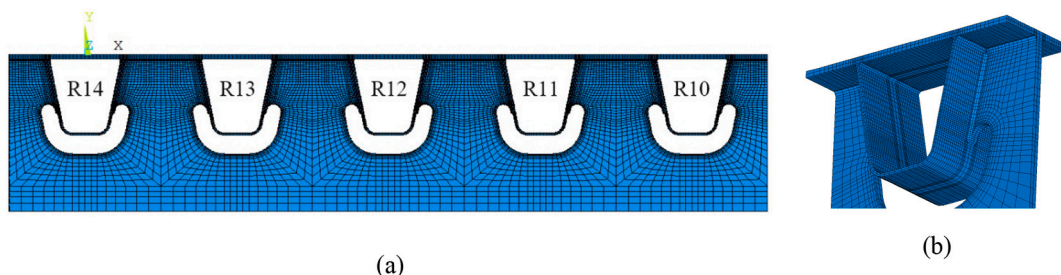


Fig. 20. Mesh arrangement: (a) OSD panel; (b) rib intersection at floorbeam and deck plate.

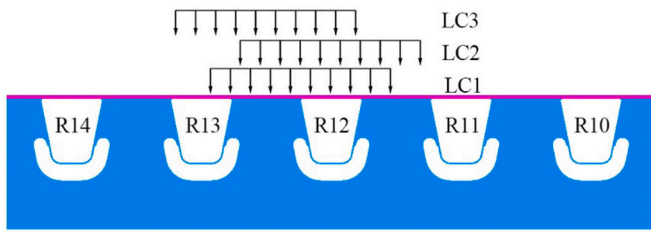


Fig. 21. Three typically transverse loading locations on panel model.

With regard to the boundary conditions applied to the panel model, three degrees of freedom were constrained for all the nodes on the boundaries, including the eastern and western longitudinal boundaries (in the Z-direction) on the deck plate, the northern and southern ends of the ribs, and the bottom, eastern, and western ends of F2, F3, and F4. It should be noted that the applied boundary conditions only approximated the real constraints from the entire structure. However, because the focus of the modeling was the RD detail at the rib span center between F3 and F4, which was located far away from the model boundaries, according to Saint-Venant’s principle, the treatment of the above boundary conditions might not have produced significant errors in the FEM results.

4.2. Loading scheme

As indicated in the controlled truck tests, in the longitudinal direction of the bridge, the length of the stress influence line at the RD detail was equal to the floorbeam spacing, i.e., 3 m for this bridge. Because the floorbeam spacing was shorter than the distance between the front and middle axles (3.8 m), only the middle and rear axles of the test truck, with their distance of 1.4 m between them, were considered in the FEM analysis. As shown in Fig. 9, considering a 70 mm thickness of the deck overlay and its load dispersal angle of 45 degrees, the wheel loads distribution area increased to 340 mm by 640 mm on the deck plate in FEM.

The controlled truck tests also indicated that for a passing truck, the stress at the RD detail generated by one side of the wheel loading was not superimposed on that produced by the other side of the wheel loading. Hence, only the left wheels of the middle and rear axles, as shown in Fig. 7, were considered for the truck loading. In addition, a dynamic load allowance of 1.05, as obtained in the controlled truck tests in this study, was applied for the dynamic consideration.

Due to limited model dimension in transverse direction, five loading cases in the field test are not applicable in FEM, as the wheel loads cannot locate too closely to the boundary condition. With this consideration, the three transverse wheel locations, frequently used as the typical loading locations in FEM analyses of an OSD [31], were selected in this study and are shown in Fig. 21. The truck running on the bridge

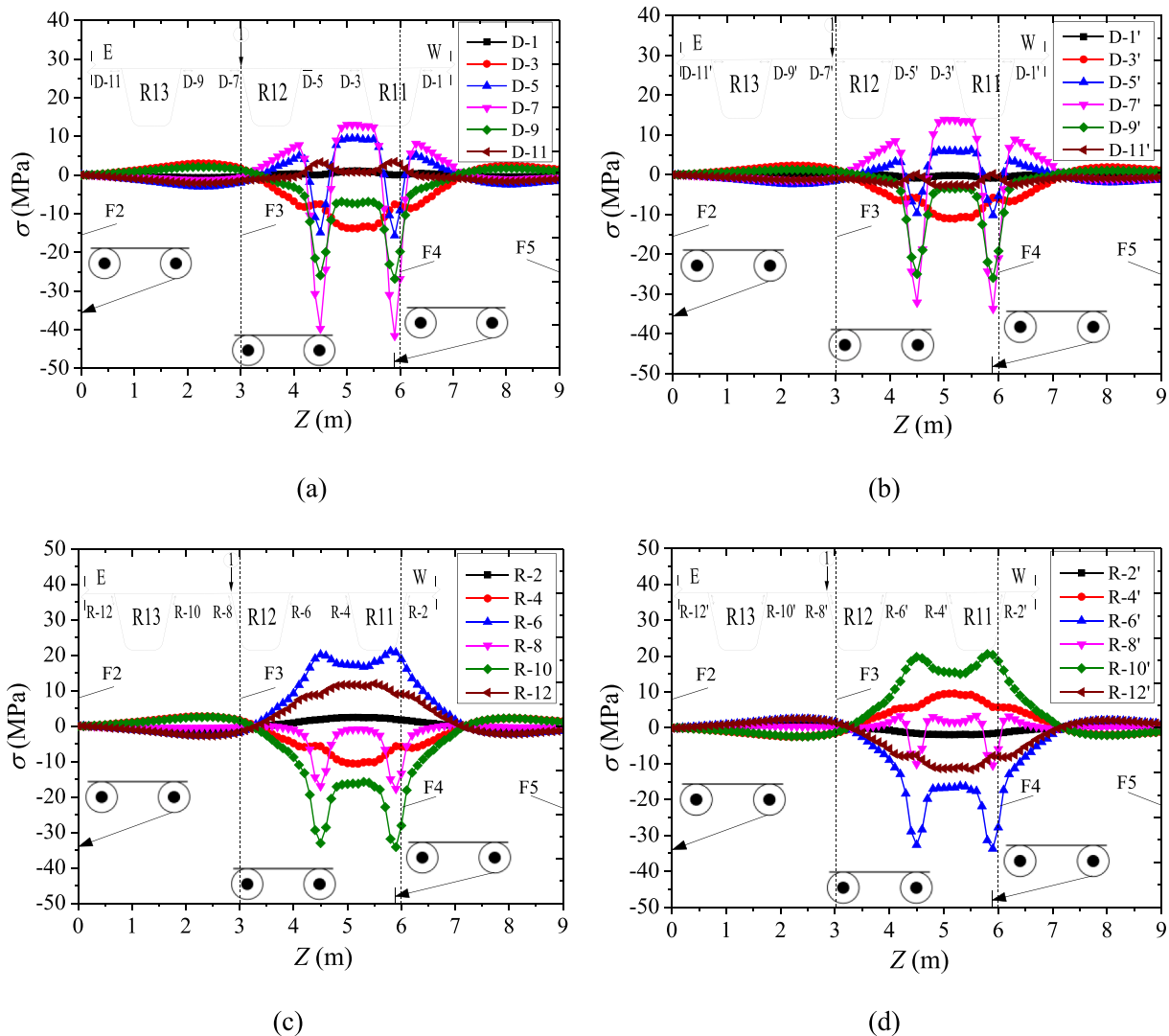


Fig. 22. Calculated stresses at RD detail under LC1: (a) RD-D (outer side); (b) RD-D (inner side) (c) RD-R (outer side); (d) RD-R (inner side).

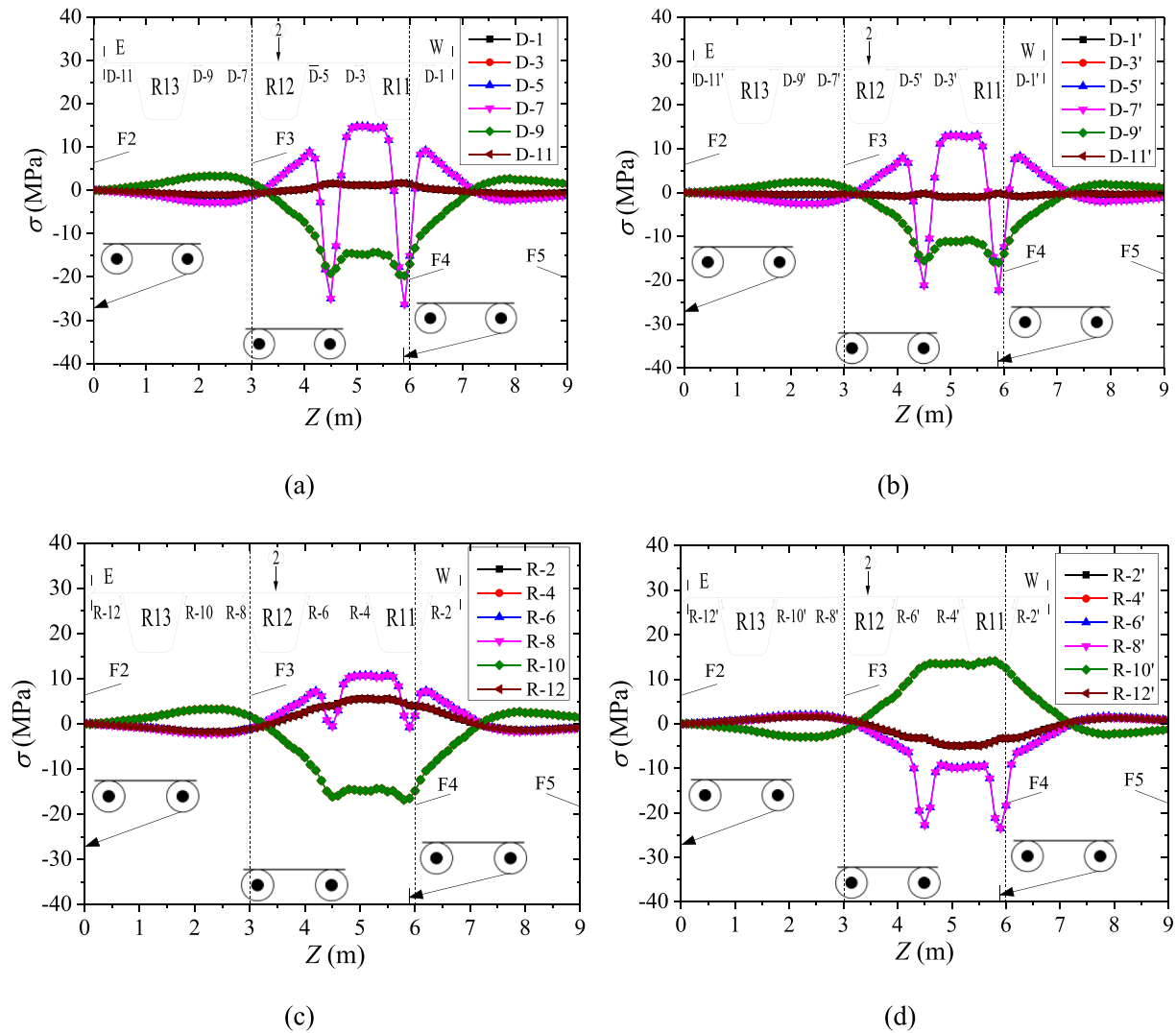


Fig. 23. Calculated stress at RD detail under LC2: (a) RD-D (outer side); (b) RD-D (inner side) (c) RD-R (outer side); (d) RD-R (inner side).

deck was modeled using a step-by-step placement of the twin axles on the panel deck with a suitable step interval in the longitudinal direction of the bridge, as shown in Fig. 19. The center of the middle axle was used to define the locations of the wheel loads in the longitudinal direction. The twin axles moved forward along the Z-axis in the positive direction with a uniform step size of 0.1 m until the middle axle reached F5 (Z = 9.0 m), which produced an array of 91 × 3 loading cases for the three transverse loading scenarios. It should be noted that the loading step size (0.1 m) in the bridge longitudinal direction was close to the identified truck loading step size in the dynamic tests based on the truck travel speed and data sampling interval.

4.3. FEM results

In order to make a direct comparison between the FEM results and those of the controlled truck tests, RD details midway between floorbeams F3 and F4 (Z = 4.5 m) were selected as the section of interest, and the stress at the RD double-sided weld detail was obtained at a location 6 mm away from the weld toes. Similar to the method used for numbering the stress gauges in the controlled truck tests, the stress points on the outer side of the RD detail in the FEM model were numbered D-3, D-5, D-7, D-9, and D-11 on the deck plate side, and R-4, R-6, R-8, R-10, and R-12 on the rib wall side. Meanwhile, the stress points on the inner side of the RD were numbered D-3', D-5', D-7', D-9',

and D-11' on the deck plate side, and R-4', R-6', R-8', R-10', and R-12' on the rib wall side, as shown in the following.

1) Loading case LC1

Fig. 22 shows the calculated stresses of the RD double-sided weld detail at five different transverse locations under LC1, where the investigated RD details were located in the middle between F3 and F4 (Z = 4.5 m). Fig. 22 (a) and (c) plot the stress curves at the outer side of the weld of the RD detail, which makes it possible to compare the results to those shown in Fig. 13 from the dynamic test. It was clear that the calculated stress curves shared almost the same trends as those from the dynamic test. The maximum responses occurred at the same location, i. e., D-7 on the deck plate side and R-10 on the rib wall side, with their maximum stress ranges of 54.6 MPa and 37.4 MPa, respectively, also in agreement with the dynamic test results. The calculated stress ranges at other outer side of the weld of the RD details were also comparable to those of the field tests. Hence, the agreement between the FEM and dynamic test results demonstrated the effectiveness of the FEM analysis.

The stress curves at the inner side of the weld of the RD detail are plotted in Fig. 22 (b) and Fig. 22 (d). Compared to the stress curves at the outer side of the weld of the RD detail, the stresses from both sides of the deck plate had the same trend, and the calculated stress ranges at D-1'-D-11' were 0.9 MPa, 13.3 MPa, 16.4 MPa, 47.6 MPa, 27.2 MPa, 3.0

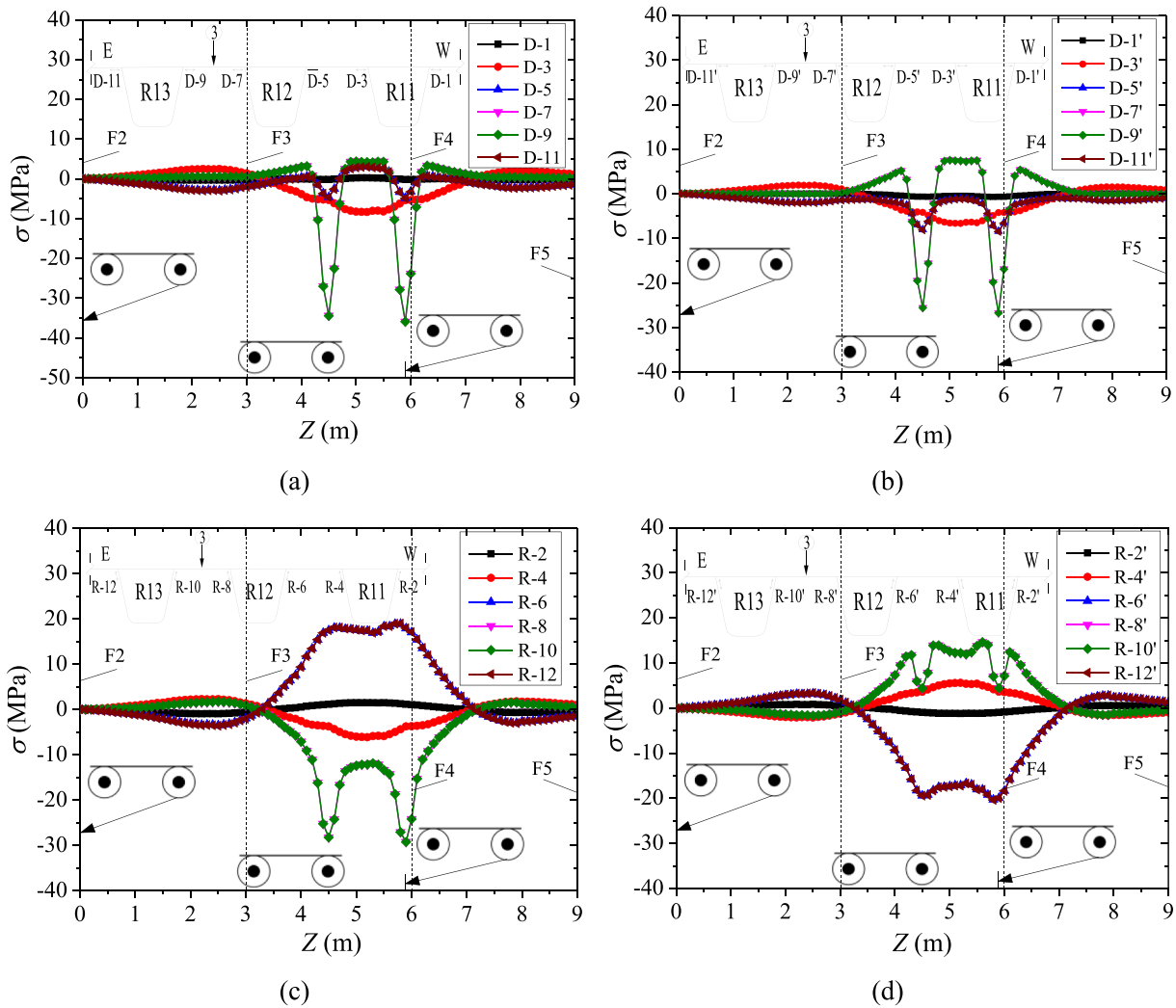


Fig. 24. Calculated stresses at RD detail under LC3: (a) RD-D (outer side); (b) RD-D (inner side); (c) RD-R (outer side); (d) RD-R (inner side).

MPa, respectively, indicating lower stress ranges than on the outer side of the weld.

The maximum stress range at the inner side of the rib wall was not only lower than that of the inner side of the deck plate, but also slightly lower than that of the outside rib wall. The calculated stress ranges at R-2–R-12 were 3.0 MPa, 12.1 MPa, 36.2 MPa, 13.9 MPa, 22.9 MPa, and 14.1 MPa, respectively. The locations of the maximum stress range were different between the inner and outer sides of the weld under this loading case. The stresses at R-8 and R-8' were all in compression because their rib walls directly supported the wheel center. For the other ribs, opposite stresses appeared on the two sides of the same rib. The maximum stress range at the outer side of the rib wall occurred at R-10 in compression, while its inner side (R-10') was in tension, indicating that the rib wall experienced out-of-plane bending. However, the maximum stress range at the inner side of the rib wall occurred at R-6' in compression, while its opposite (R-6) was in tension. Hence, if the rib wall was offset to the wheel center, it would suffer out-of-plane bending.

2) Loading case LC2

In this loading case, the wheel load was symmetrical to the center line of R12; hence, symmetrical locations at the deck plate and rib wall were expected to have identical responses under the passage of wheel loads, as shown in Fig. 23. The maximum stress range appeared at D-5 and D-7 on the outer side of the weld on the deck plate, which was

underneath the truck wheel, but this maximum stress range was lower than that of LC1. The stress ranges at the outer side of the weld on the deck plate were 2.8 MPa, 23.1 MPa, 41.1 MPa, 41.1 MPa, 23.1 MPa, and 2.8 MPa at D-1–D-11, respectively, while the stress ranges at the inner side of the deck plate were 1.1 MPa, 18.4 MPa, 35.4 MPa, 35.4 MPa, 18.4 MPa, and 1.0 MPa at D-1'–D-11', respectively. The stress curves at both sides shared the same trend, although the stress ranges at the inner side of the weld on the deck plate were 14% smaller than those on the outer side of the weld on the deck plate.

The stress ranges at the outer side of the weld on the rib wall were 7.4 MPa, 20.1 MPa, 13.0 MPa, 13.0 MPa, 20.1 MPa, and 7.4 MPa for R-2–R-12, respectively, while they were 6.6 MPa, 17.1 MPa, 25.4 MPa, 25.4 MPa, 17.1 MPa, and 6.6 MPa for R-2'–R-12', respectively, at the inner side of the weld on rib wall. Although the maximum stress range at the inner side of the weld on the rib wall was higher than that on the outer side of the weld on the rib wall, it was significantly lower than the maximum stresses on both sides of the deck plate.

3) Loading case LC3

Fig. 24 illustrates the stress curves at the RD detail under this transverse loading case, where the wheel centers were between ribs R12 and R13. A comparison between Fig. 24 (a) and (b) indicates that the inner side and corresponding outer side of the weld on the deck plate had almost the same stress curves, although the stress ranges at the inner

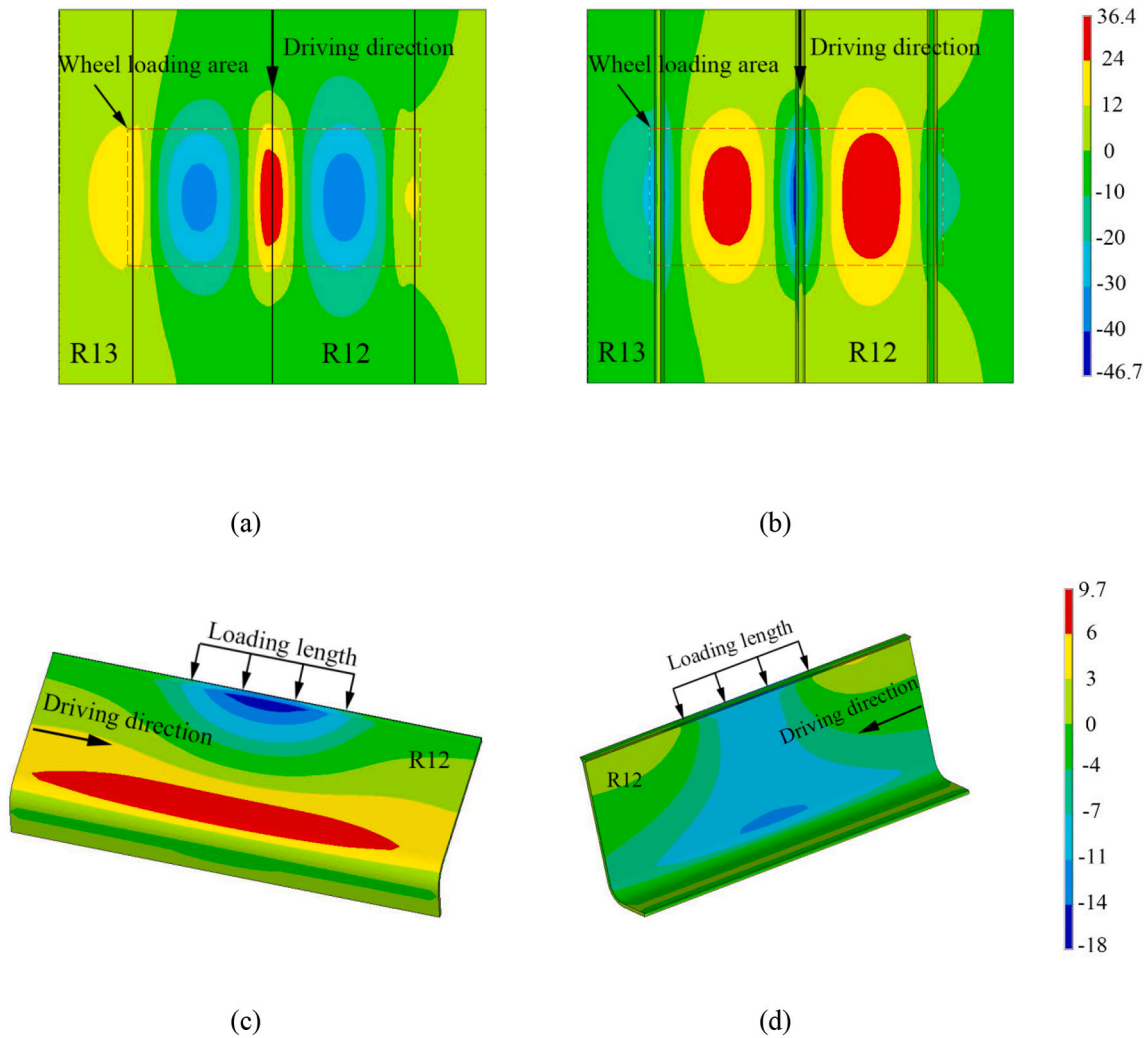


Fig. 25. Stress contour plots of RD detail around R12 under LC1 (Unit: MPa): (a) deck plate top surface; (b) deck plate bottom surface; (c) rib outside surface.

side were lower than the corresponding values on the outer side, with maximum stress ranges of 40.3 MPa and 34.3 MPa occurring at the outer side and inner side of the weld on the deck plate, respectively. In addition, the stress curves in Fig. 24 (a) indicate two clearly separated individual stress peaks.

The stress ranges at the outer side of the rib wall were 2.5 MPa, 8.4 MPa, 22.4 MPa, 30.9 MPa, 31.0 MPa, and 22.6 MPa at R-2-R-12, respectively, while those at the inner side of the weld on the rib wall were 2.0 MPa, 7.7 MPa, 23.6 MPa, 16.2 MPa, 16.3 MPa, and 23.7 MPa at R-2'-R-12' respectively. Again, the maximum stress range at the inner side of the weld on the rib wall was lower than that on the outer side of the weld on the rib wall, and it was significantly lower than the maximum stress range produced at the deck plate side.

Based on the FEM results, an important observation was that the apparent stress response could only be produced at the RD detail of interest ($Z = 4.5$ m) when the truck wheel loaded on the rib span, while the stress at the detail was small if the truck wheels crossed the floor-beam (F4 shown in Figs. 22–24) and moved away from the rib span. Hence, in the longitudinal direction of the bridge, the length of the stress influence line was equal to the floorbeam spacing, i.e., 3 m for the box girder. This confirmed the results of the dynamic tests. In addition, for the RD double-sided weld detail, when the transverse distance from a detail to the wheel center did not exceed the spacing between ribs (0.6 m for this box girder), a large stress was produced at that detail. With an increase in this distance, the stress response at that detail decreased,

such as D-1/1', D-11/11', R-2/2', and R-12/12' in LC1; D-1/1', D-11/11', R-2/2', and R-4/2' in LC2; and D-1/1', D-3/11', R-2/2', and R-4/4' in LC3; as shown in Figs. 22–24. Hence, the stress at the RD double-sided weld detail was highly dependent on its distance from the wheel center, both in the longitudinal and transverse directions, i.e., there were significant local stress effects under wheel loads.

The FEM results also revealed that if the RD double-sided weld detail was underneath the deck plate covered by the wheel load distribution width, the effects of individual axles could clearly be identified at the RD detail, with each axle producing an individual stress cycle. However, if an RD double-sided weld detail was outside the wheel load distribution width, it was only possible to identify the axle group, which also confirmed the findings of the controlled truck tests.

4.4. Discussion

The FEM results made it easier to understand the OSD panel behaviors such as the local stress effects and three-dimensional deformation under different transverse wheel loadings.

1) Local stress under wheel loads

Figs. 25–27 show the stress contours on the model between F3 and F4 ($Z = 4.5$ m) with the middle axle loaded at the three typical transverse loading locations shown in Fig. 21. The displayed stress component was

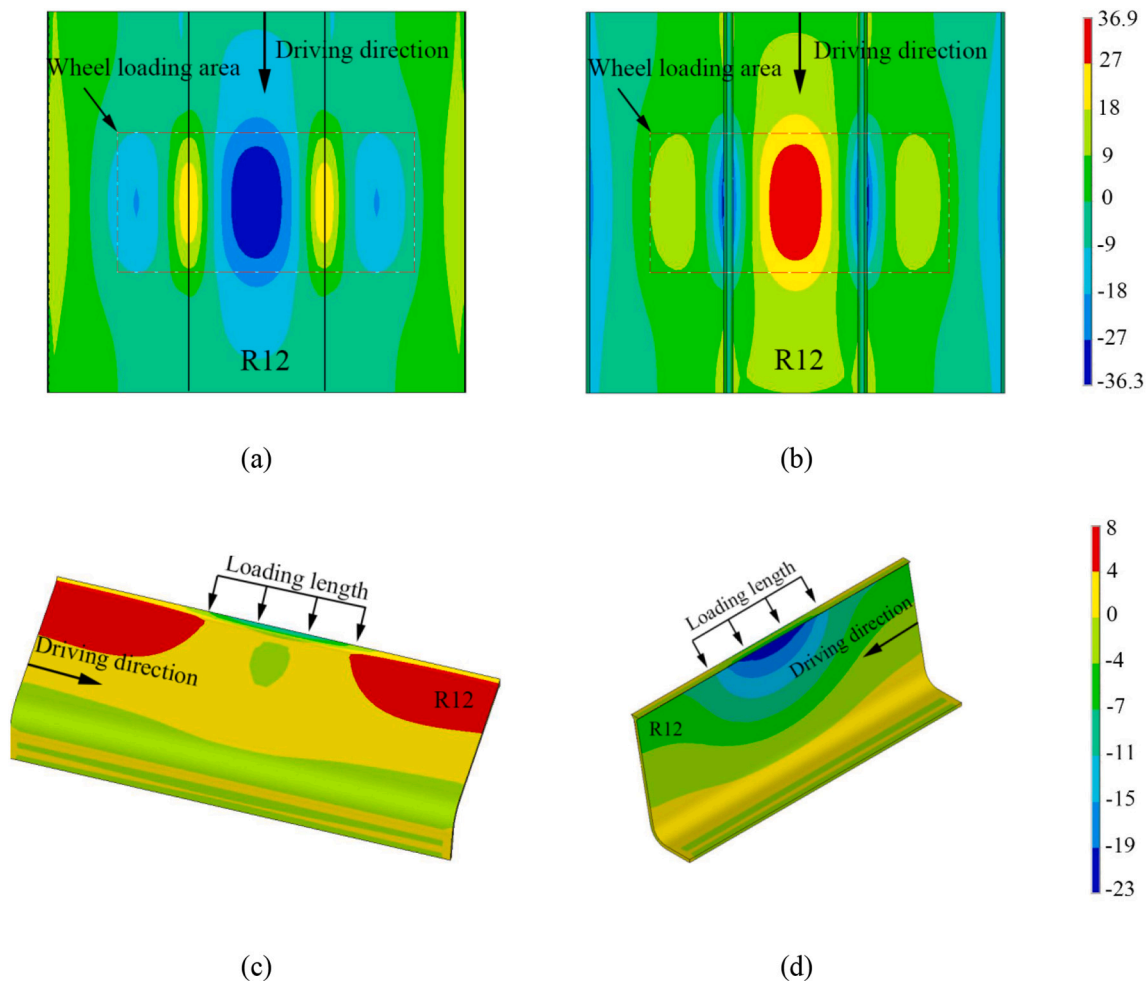


Fig. 26. Stress contour plots of RD detail around R12 under LC2 (Unit: MPa): (a) deck plate top surface; (b) deck plate bottom surface; (c) rib outside surface; (d) rib inner surface.

in the bridge transverse direction (i.e., normal to the RD weld toe). Apparently, high stress appeared at the deck plate, which was directly underneath the wheel loads, and a significant stress concentration was generated at the RD detail. The local stress effects, in which the deck plate behaved similar to a continuous beam supported by the rib walls, as mentioned in Section 1, were quite evident. On the top surface of the deck plate, the area near the RD weld was in tension, while the other area was in compression, whereas the stress distribution on the deck plate's bottom surface was completely reversed. The stress distributions on the inner and outer sides of the weld on the rib wall were not the same, implying that the rib did not behave similar to a longitudinal beam deflecting in the vertical direction. In other words, additional deformation might occur and be coupled with rib deflection.

As shown in Fig. 25 (a), the wheel load was centered on the RD weld and distributed on both sides of the deck plate at the weld; hence, clockwise and counterclockwise moments were produced on the deck plate. Accordingly, transverse compressive stress would be generated on the deck plate's bottom surface at the RD detail. The stress at this location was the sum of the stress produced by the global effects on the deck plate and that generated by the local effects under the wheel load. The dominant compressive stress on the top surface of the deck plate suggested that the local effects at the deck plate were significantly larger than the global effects under wheel loading. This strongly supports the idea that the OSD panel model created using the FEM is feasible for investigating the stress at the RD detail under wheel loads.

When the wheel was centered on the rib wall (LC1), the rib wall was directly underneath the wheel center; hence, the rib wall acted as a

support for the wheel loads. Consequently, the stress at this rib wall (1–8, R-8') would be in compression. This explained why the highest stress was generated at 1–7 and D-7, while lower stresses were produced at 1–8 and R-8'. On the eastern and western sides of the wheel center under LC2 and LC3, the stress distributions at the RD details were almost the same, which implied that the wheel load was almost equally supported by both sides of the rib wall, as shown in Fig. 26 and Fig. 27. Hence, the stress response at the RD detail definitely decreased at the two loading locations. This partly explained why LC1 was the most critical transverse loading location for the RD.

2) Three-dimensional deformation

Fig. 28 plots the cross-sectional deformation and von Mises stress contour of the panel model midway between F3 and F4 ($Z = 4.5$ m) at the three typical transverse loading locations. The deformation was characterized by differential deflection between the five ribs and deck plate bending, as well as rib wall warping and distortion, which was highly dependent on the wheel location on the deck. If the ribs were directly underneath or adjacent to the wheel load, their deflection was large, whereas if they were far away from the wheel load, their deflection was small or even negligible. This differential deflection between ribs, coupled with the rib wall bending produced by offset wheel loads, produced significant rib warping and distortion, particularly for these ribs underneath or adjacent to the wheel, such as R11, R12, and R13, as shown in Fig. 28. In addition, such rib distortion would result in a complicated secondary stress in the rib walls, as shown in Figs. 25–27.

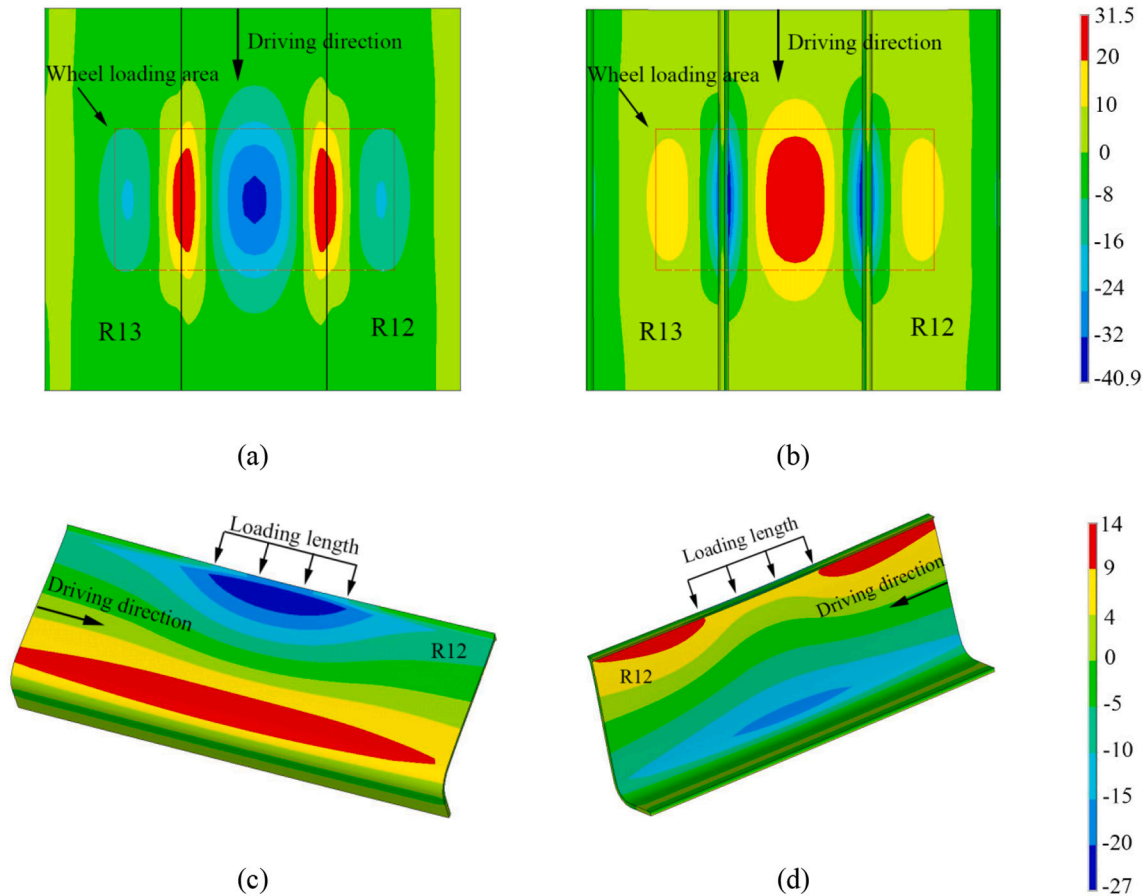


Fig. 27. Stress contour plots of RD detail around R12 under LC3 (Unit: MPa): (a) deck plate top surface; (b) deck plate bottom surface; (c) rib outside surface; (d) rib inner surface.

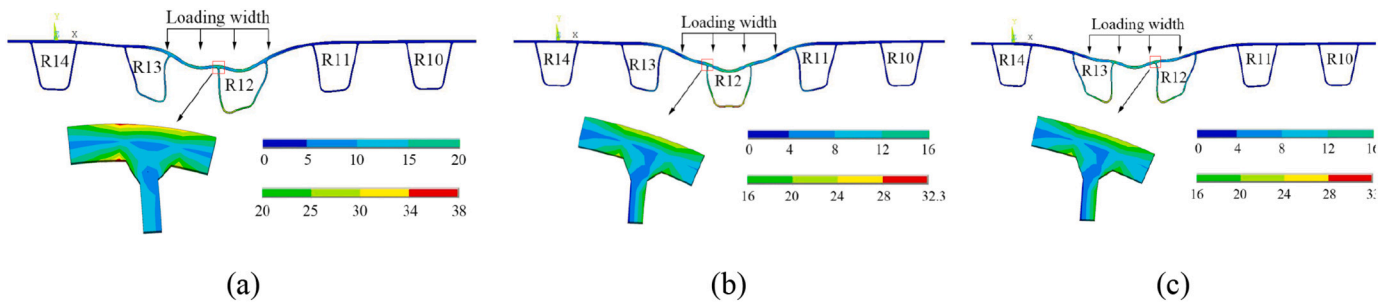


Fig. 28. Cross-sectional deformations of deck panel model and von Mises stress contour plots (Unit: MPa): (a) LC1; (b) LC2; (c) LC3.

Fig. 29 displays the three-dimensional deformation of the panel model under LC1, where the middle axle was also midway between F3 and F4 ($Z = 4.5$ m). Because of the concentrated wheel loads and lower bending stiffness of the deck plate, simultaneous longitudinal and transverse deformations appeared under the wheel loads (Fig. 29 (a) and Fig. 29 (b)), which were clearly three-dimensional. The clearly illustrated dimple under the wheel loads shows the low stiffness of the deck plate in the vertical direction. Meanwhile, ribs warping and deflection also occurred under wheel loading (Fig. 29 (b) and Fig. 29 (c)), which would produce out-of-plane bending at the floorbeam cutout detail, and fatigue cracks were observed at the cutout detail on several OSD bridges [2].

5. Conclusions and remarks

Based on controlled truck loading tests and FEM analyses, this study conducted an extensive investigation of the stress behaviors at RD double-sided weld details. The following conclusions and remarks can be made.

- 1) The RD double-sided weld details showed significant local stress effects from wheel loads. When their distances to the wheel center did not exceed the rib spacing in the transverse direction, apparent stresses at those locations were produced. Otherwise, the stress was small or even negligible. Hence, for a passing truck, the stress at the RD detail generated by one side of the wheel was not superimposed on that from the other side of the wheel. In particular, the loading effects produced by trucks running side-by-side could be ignored.

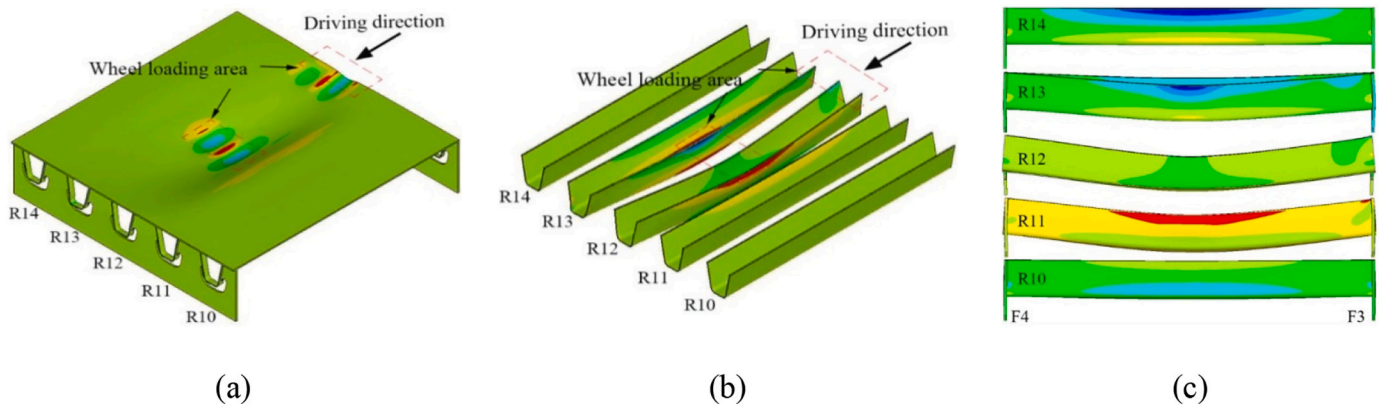


Fig. 29. Three-dimensional deformation of deck panel model under LCI: (a) oblique view; (b) rib warping; (c) rib deflection.

- In the longitudinal direction of the bridge, the wheel loading effects at an RD double-sided weld detail could be discerned only when the wheels were loaded on the RD detail-affiliated rib span. In addition, each axle could produce an individual stress cycle at the RD detail only when the detail was underneath the deck plate covered by the wheel load distribution width.
- Among the three typical transverse loading locations, riding-rib-wall loading was the most critical loading location for the RD double-sided weld detail, with the highest stress range at the deck plate.
- The ribs could suffer from complicated deformations, including differential deflection, warping, and distortion, which were highly dependent on the wheel location in both the longitudinal and transverse directions.
- The maximum stress range produced on the outer side of the weld of an RD detail was higher than that on the inner side. Hence, stress measurement on the outer side of the weld of a RD detail could conservatively be used for the fatigue life evaluation of existing OSD bridges with RD double-sided weld details.
- The dynamic load allowance of 15%, as specified in AASHTO LRFD for fatigue limit state, may be conservative based on stress measurement at the RD detail.

Data availability statement

Some or all data, models, or code that support the findings of this study are available from the corresponding author upon reasonable request.

Declaration of Competing Interest

The authors declare that they have no known competing financial interests or personal relationships that could have appeared to influence the work reported in this paper.

Acknowledgements

This study was supported by the National Natural Science Foundation of China (grant number 51878269), for which the authors are grateful.

References

- Federal Highway Administration (FHWA), US Department of Transportation, Manual for Design, Construction and Maintenance of Orthotropic Steel Deck Bridges, FHWA, Washington, D.C., 2012.
- Z. Zhu, Z. Xiang, J. Li, Y. Huang, S. Ruan, Fatigue behavior of orthotropic bridge decks with two types of cutout geometry based on field monitoring and FEM analysis, *Eng. Struct.* 209 (2019) 109926.
- R. Wolchuk, Lessons from weld cracks in orthotropic decks on three European bridges, *J. Struct. Eng.* 116 (1) (1990) 75–84.
- F.B.P. De Jong, Overview Fatigue Phenomenon in Orthotropic Bridge Decks in the Netherlands, The First Orthotropic Bridge Conference Proceedings, ASCE, Washington DC, 2004, pp. 489–512.
- A.F. Hobbacher, Recommendations for Fatigue Design of Welded Joints and Components, 2nd edn, 2019.
- Z. Fu, B. Ji, C. Zhang, Q. Wang, Fatigue performance of roof and U-rib weld of orthotropic steel bridge deck with different penetration rates, *J. Bridg. Eng.* 22 (6) (2017), 04017016-1-12.
- M. Li, Y. Suzuki, K. Hashimoto, K. Sugiura, Experimental study on fatigue resistance of rib-to-deck joint in orthotropic steel bridge deck, *J. Bridg. Eng.* 23 (2) (2017), 04017128-1-10.
- P.A. Tsakopoulos, J.W. Fisher, Full-scale fatigue tests of steel orthotropic decks for the Williamsburg bridge, *J. Bridg. Eng.* 8 (5) (2003) 323–333.
- H. Sim, C. Uang, Stress analyses and parametric study on full-scale fatigue tests of rib-to-deck welded joints in steel orthotropic decks, *J. Bridg. Eng.* 17 (5) (2012) 765–773.
- S. Ya, K. Yamada, T. Ishikawa, Fatigue evaluation of rib-to-deck welded joints of orthotropic steel bridge deck, *J. Bridg. Eng.* 16 (4) (2011) 492–499.
- American Association of State Highway and Transportation Officials (AASHTO), AASHTO LRFD Bridge Design Specifications, 7th edn., AASHTO, Washington, D.C., 2014.
- BS5400, Code of Practice for Fatigue, 1980.
- JRA, Fatigue Design Specifications for Steel Bridges, Japan Road Association, Tokyo, 2002.
- C. Wang, B. Fu, Q. Zhang, Y. Feng, Fatigue test on full-scale orthotropic steel bridge deck, *China J. Highw. Transp.* 26 (2) (2013) 69–76.
- P.A. Tsakopoulos, J.W. Fisher, Full-scale fatigue tests of steel orthotropic deck panel for the Bronx-Whitestone bridge rehabilitation, *Bridg. Struct.* 1 (1) (2005) 55–66.
- S. Kainuma, M. Yang, Y.S. Jeong, S. Inokuchi, D. Uchida, Experimental investigation for structural parameter effects on fatigue behavior of rib-to-deck welded joints in orthotropic steel decks, *Eng. Fail. Anal.* 79 (2017) 520–537.
- C. Cui, Q. Zhang, Y. Bao, S. Han, Y. Bu, Residual stress relaxation at innovative both-side welded rib-to-deck joints under cyclic loading, *J. Constr. Steel Res.* 156 (2019) 9–17.
- P. Feng, K. Fu, Y. Chen, Key techniques of design of main bridge of Zhuankou Changjiang river highway bridge, *China J. Bridg. Constr.* 47 (2) (2017) 7–12.
- H. Chen, J. Zhang, M. Liu, W. Ding, H. Shen, Overall design of main bridge of Shishou Changjiang river highway bridge, *China J. Bridg. Constr.* 47 (5) (2017) 6–11.
- Q. Zhang, Y. Guo, J. Li, D. Yuan, Y. Bu, Fatigue crack propagation characteristics of double-sided welded joints between steel bridge decks and longitudinal ribs, *China J. Highw. Transp.* 32 (7) (2019) 49–56.
- P. Luo, Q. Zhang, D. Gong, Y. Bu, Z. Ye, Study of fatigue performance of U rib-to-deck double-sided welded joint in orthotropic steel bridge deck, *China J. Bridg. Constr.* 48 (2) (2018) 19–24.
- Y. Liu, F. Chen, N. Lu, L. Wang, B. Wang, Fatigue performance of rib-to-deck double-sided welded joints in orthotropic steel decks, *Eng. Fail. Anal.* 105 (11) (2019) 127–142.
- R. You, P. Liu, D. Zhang, J. Feng, A. Zhu, Study on fatigue performance of U rib-to-deck connection with double sides welding in orthotropic steel bridge deck, *J. China & Foreign Highw.* 38 (3) (2018) 174–179.
- Q. Zhang, J. Li, D. Yuan, J. Zhu, C. Cui, Fatigue performance of high fatigue resistance orthotropic steel bridge deck I: model test, *China J. Highw. Transp.* 34 (3) (2021) 124–135.
- Q. Zhang, D. Yuan, B. Wang, R. Han, J. Li, Fatigue performance of innovative both-side welded rib-to-deck joint, *China J. Highw. Transp.* 32 (7) (2019) 49–56.
- Z. Zhu, T. Yuan, Z. Xiang, Y. Huang, Y.E. Zhou, X. Shao, Stress behaviors and fatigue performance of details in orthotropic steel bridges with UHPC-deck plate composite system under in-service traffic flows, *J. Bridg. Eng.* 23 (3) (2018), 04017142.

- [27] P.A. Tsakopoulos, J.W. Fisher, Williamsburg Bridge Replacement Orthotropic Deck as-Built Full-Scale Fatigue Test: Final Rep. on Phase 2B. ATLSS Rep. No. 99-02, ATLSS, Bethlehem, PA, 1999.
- [28] R.J. Connor, J.W. Fisher, Results of Field Measurements Made on the Prototype Orthotropic Deck on the Bronx-Whitestone Bridge-Final Report, ATLSS Report No. 04-03, Center for Advanced Technology for Large Structural Systems, Lehigh University, Bethlehem PA, 2004.
- [29] H. Hou, T. Wang, S. Wu, Y. Xue, R. Tan, J. Chen, M. Zhou, Investigation on the pavement performance of asphalt mixture based on predicted dynamic modulus, *Constr. Build. Mater.* 106 (2016) 11–17.
- [30] Z. Zhu, Z. Xiang, Y.E. Zhou, Fatigue behavior of orthotropic steel bridge stiffened with ultra-high performance concrete layer, *J. Constr. Steel Res.* 157 (2019) 132–142.
- [31] Z. Xiao, K. Yamada, S. Ya, X. Zhao, Stress analyses and fatigue evaluation of rib-to-deck joints in steel orthotropic decks, *Int. J. Fatigue* 30 (8) (2008) 1387–1397.